RESEARCH ARTICLE

WILEY

Large eddy simulation: A study of clearings in forest and their effect on wind turbines

Johanna Matsfelt [ID] | Lars Davidson [ID]

Division of Fluid Dynamics, Department of Mechanics and Maritime Sciences, Chalmers University of Technology, Gothenburg, SE-412 96, Sweden

Correspondence
Johanna Matsfelt, Division of Fluid Dynamics, Department of Mechanics and Maritime Sciences, Chalmers University of Technology, SE-412 96 Gothenburg, Sweden.
Email: johanna.matsfelt@chalmers.se

Abstract

In this article, the Ryningsnäs site in Sweden is investigated using large eddy simulation with three different clearing setups: a homogeneous forest, that is, no clearing, the current clearing, that is, the existing clearing at the location, and an extended clearing. Neutral stratification is simulated, and the wind turbines are modelled by a two-way-coupled actuator line model. From the simulations, the electrical generator power was found to be the highest for the current clearing. But the fatigue loads were both higher and lower than the homogeneous forest depending on which part of the wind turbine that was investigated. The extended clearing nearly always had the lowest fatigue loads but unfortunately also the lowest electrical generator power. Further optimization of the clearings and the wind turbine locations in relation to them is needed to find the sweet spot where the fatigue loads are lower and the electrical generator power is higher.

KEYWORDS
ALM, CFD, forest clearing, LES, OpenFOAM, SOWFA, wind turbine

1 | INTRODUCTION

When the number of wind farms increases, the number of wind turbines placed in forested areas will also increase, because of the large forest areas in Sweden. The wind turbines placed in forested areas experience a drastic increase in the fatigue loads, so their maintenance costs increase making them less profitable.[1,2] In this work, clearings in forest are studied to be able to increase the electrical power generated by the wind turbines and decrease the fatigue loads to make them more profitable. The approach in this work is to use computational fluid dynamics (CFD). We use the method large eddy simulation (LES). The CFD simulation is coupled to an aero elastic solver that solves the dynamic response of the wind turbine.

1.1 | Clearings in forest regions

When a forest edge is present, the flow field is changed dramatically compared to a fully homogeneous forest. LES of a forest edge flow has been made by Mueller et al.[3] in their study and compared to results using static inlet boundary condition and dynamic inlet boundary condition from a precursor simulation. The dynamic inflow condition outperformed the static, and the recommendation was that the static inflow condition should be avoided. Measurements with wind from an open landscape meeting a forest edge has been performed by Dellwik et al.[4] The data were taken at 1.5 forest heights inside the forest at leaf-off and leaf-on with leaf area index (LAI) of 1 and

6, respectively. The total kinetic energy was generally higher during the leaf-on period than at the leaf-off period. The reason was assumed to be the higher roughness of the upstream landscape during this period. In both cases, the total kinetic energy was unchanged when the flow moved over the forest edge and to the measurement location. The momentum flux was largest at the open landscape location which is somewhat surprising.

Dupont et al.[5] compare measurements with simulations where a flow is meeting a forest edge and developing over the forest for two forest cases with LAI of 2 and 5. The simulation results agree with the trends in the measurements at 1.5 forest heights inside the forest. The computational domain is longer than the distance covered by the measurements, making it able to provide more information when the flow is developing further along the forest. In both forest types, the total kinetic energy and the momentum flux are increased as the flow is moving along the forest, with the highest LAI forest showing the highest values of the two. A neutrally stratified forest edge flow was studied using RANS by Sogachev et al.[6] and using LES by Kanani et al.[7] for LAI ranging from one to eight and velocity at 10 m ranging from 1.8 to 7.2 m/s. In both papers, they showed that the scalar accumulation is partly due to the converging of the streamwise mean flow. The scalar fluxes showed a peak downstream of the forest edge, which moved closer to the forest edge and increased in size as the LAI increased. This is due to the higher drag force from the forest and similar to the behaviour of the concentration peak. When the wind speed was decreased, the flux peak remained unchanged while the concentration peak increased.

The distance from the forest edge that the flow is affected was studied by Dupont et al.,[8] and results showed that edge effects were significant about 22 forest heights after the edge. The affected distance could be even larger for scalar quantities such as temperature because they need a larger distance than the velocity to adjust.[9] The large affecting distance after the forest edge shows that forests with clearings streamwise greater than five forest heights will always show edge effects. This is due to the formation of a sub-canopy wind jet at the leading edge in forests with clearings.[10] When the clearing is in the form of a lake, it has been shown that the turbulent mixing was mostly due to the wind shear at the tree height of the canopy rather than the thermal stratification due to the lake.[11]

1.2 | Forest in complex terrain

When comparing computations assuming horizontal homogeneity to measurements, the wind profiles seemed to agree,[12] but the third order moment showed that there may be some terrain dependence.[13] This showed that further studies are needed to find the dependency of the turbulence in the forest on the complex terrain. When LES were compared to wind tunnel experiments of the flow over a forested 2D hill,[10] the validation showed that the model could accurately reproduce the flow characteristics. Dupont et al. used the k-ε turbulence model in their study[14] to perform 2D and 3D simulation of a forested park damaged by a windstorm. From the 2D simulations of a vertical section of the park, it was observed that a region of turbulence always develops at a distance from the leading edge of the forest, but the distance depends on the heterogeneity of the forest. If the forest is heterogeneous both vertically and horizontally, the strong wind shear at the top of the canopy is weakened and thereby also the turbulence region caused by it compared to a homogeneous forest. The simulations also showed that the intensity of the turbulence increased when the forest was denser during the summer, that is, high LAI values. The 3D simulations of the entire park show that the distance from the leading edge where the flow develops depends on the spatial heterogeneity of the canopy. It could thereby not be classified as a constant distance from the leading edge for the entire park. The simulations could point out the regions of the strongest turbulence levels, and these seemed to agree with the damaged areas. This also showed that the damage in the forest was due to the wind characteristics. This assumption was also strengthened by a study that the damage could not be consistent with any other environmental factor. The authors pointed out that the physics of the model could not provide information about any instantaneous turbulent quantities. They also showed a strong interest in simulating turbulent flow in complex terrain over a strongly heterogeneity forest.

Mohr et al. obtained data from an airborne laser scan in their study[15] to calculate the forest heights and the plant area index from a newly developed model. It was compared to the official estimates by the Swedish Forest Agency and showed good agreement. They suggested that the data given by the Swedish Forest Agency are good to use because they are constantly updated for new clearings. Ivanell et al. asked different modellers to compute the wind profile at Ryningsnäs from three different directions in their study.[16] The modellers were given forest densities and topology of the ground from an airborne laser scan. The Meteodyn model did not use these given data and stands out in the comparison. The authors do however point out that the difference also to some extent can be due to the different turbulence closure. OpenFOAM using LES performs very well when predicting the shear, while most of the models overpredicts the shear. The authors believe that this could be due to how the airborne laser scan data are used to predict the forest densities. In the study, two participants using LES models took part. The LES results using the lower resolution, and the larger computational domain had the best agreement with the measurements. They concluded that the computational domain has to be in the order of 20 km to accurately reproduce the footprint on the sampling location caused by the upstream topology and forest. The authors pointed out the importance of not normalizing the results because the importance of the forest density and topology would give different fetches for different wind speed and turbulence.

1.3 | Forest modelling

The forest can be modelled in many ways. One example is to represent it by the roughness of the wall model.[17] A more complex way is to simulate it by using a drag and heat source as has been implemented in the work covered by this article.[18]

$$F_{f,i} = -C_{Df} a_f U \bar{u}_i \tag{1}$$

Equation (1) shows the added term to the momentum equation, that is, the drag force of the forest. C_{Df} is the drag force coefficient of the forest, and it is set to 0.15.[18] The vertical leaf area density a_f is supposed to simulate the shape of the drag force of the simulated forest. An illustration can be seen in Figure 1.

The heat source in the potential temperature equation is computed in eq. (2). To represent the heat source in the forest the extinction coefficient of light, γ, is set to 0.6.[18] The canopy heat source Q_h is dependent on which kind of atmospheric stability is simulated.

$$S_h = \frac{\partial}{\partial z}(Q_h exp(-\gamma A_c)) \tag{2}$$

The area leaf density seen in eq. (2) is evaluated using eq. (3). It is the total vertical leaf density of the forest. The vertical leaf area density a_f can be obtained in numerous ways. One way is to measure it in the forest. Another way that has been used here and can be seen in eq. (4) is to obtain it from an empirical formula.[19]

$$A_c = \int_z^h a_f dz \tag{3}$$

In eq. (4), the shape of the forest is determined by the parameters n, L_m and z_m. The n parameter has been evaluated in different ways by different developers; here eq. (5) is used and has been shown to properly evaluate n.[19] The L_m and z_m parameters on the other hand are dependent on which kind of forest that is evaluated.[18,19] The L_m parameter describes the maximum leaf area density, and z_m is the height at which L_m occurs.

$$a_f(z) = L_m \left(\frac{h-z_m}{h-z}\right)^n exp\left(n\left(1-\left(\frac{h-z_m}{h-z}\right)\right)\right) \tag{4}$$

$$n = \begin{cases} 6 & 0 \leq z < z_m, \\ \frac{1}{2} & z_m \leq z \leq h \end{cases} \tag{5}$$

1.4 | Actuator turbine models

When simulating wind turbines in CFD, actuator turbine models are often used in favour of solving the flow field over each blade. The main advantage of this is that the boundary layer on each blade does not need to be resolved so the mesh resolution can be reduced significantly.[20] The actuator turbine models is based on the blade element momentum method (BEM) which calculates the forces on the blades modelled as 2D airfoil profiles. The wind turbine is then simulated by lift and drag forces by using the C_L and C_D from 2D airfoil tables and assuming constant cord length of each section of the blades.
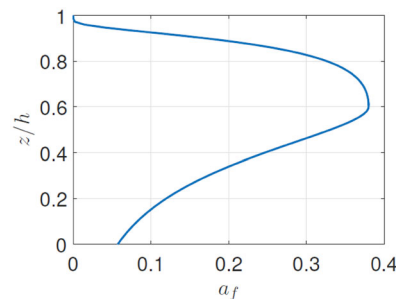

FIGURE 1 Example of the vertical leaf area density profile

1.4.1 | Actuator disk model

Actuator disk model (ADM) is an actuator turbine model that simulates the effect of the time-averaged swept area of the blades as a disk; an illustration can be seen in Figure 2.

$$F_i^{ADM} = \left(L_i^{ADM}, D_i^{ADM}\right) = \frac{B}{2\pi r}\frac{1}{2}\rho U_{rel}^2 c(C_L e_L, C_D e_D) \tag{6}$$

In ADM the lift and drag forces are per unit area as can be seen in eq. (6) as L_i^{ADM} and D_i^{ADM}.[21] An example of an area section where the force from an ADM routine could be applied on can be seen in Figure 3. Equation (6) is a modified lift and drag force equation for an airfoil now used to represent the forces exerted by the blades on the wind flow. Further information on the steps from BEM to ADM can be found in the PhD thesis by Mikkelsen.[21]

1.5 | Actuator line model

Actuator line model (ALM) is used in the present study. In ALM, the blades are simulated as lines; an illustration can be seen in Figure 2.

$$F_i^{ALM} = \left(L_i^{ALM}, D_i^{ALM}\right) = \frac{1}{2}\rho U_{rel}^2 c(C_L e_L, C_D e_D) \tag{7}$$

The ALM formula for lift and drag can be seen in eq. (7), as L_i^{ALM} and D_i^{ALM}. Compared to the ADM, the ALM formula has the unit force per meter instead of force per area. ALM can capture the tip and root vortices which ADM cannot.[22] To represent these vortices is important when
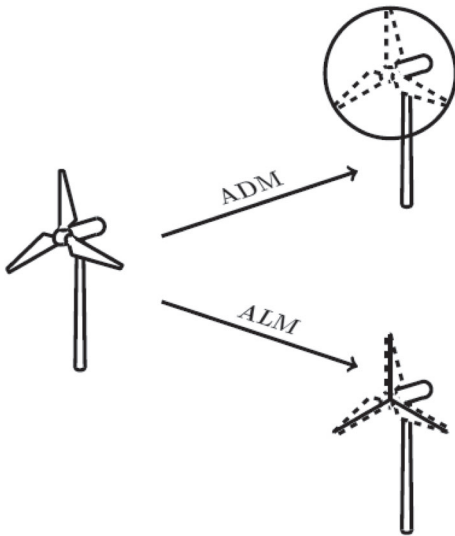

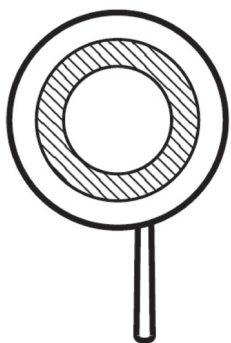FIGURE 2   Simulation of wind turbine blades in ADM and ALM

FIGURE 3   Area sections of ADM

studying the near wake and is a clear advantage of the ALM over the ADM. The advantage of ADM compared to ALM is the simulation time.[22] This is because the actuator lines of ALM should not travel through too many cells each time step, preferably only on cell.[20,22] Hence, the time step for ALM must be much smaller than for ADM.

1.6 | Coupling actuator turbine models and CFD

Actuator turbine models can be used in CFD in two ways. The first one is called one-way coupling where the flow field of the CFD is fed in to the actuator turbine model and evaluated. The second way is to feed the forces obtained by the actuator turbine model back to the CFD, this is called two-way coupling, which is used in the present study. To do this, a Gaussian distribution is used to smear the force in the neighbourhood of the actuator point. This is necessary in order to avoid numerical oscillations in the simulation that otherwise will occur.[17] The way the forces in the Gaussian is smeared in the neighbourhood of the actuator point can be done in many different ways. In ADM, a 1D Gaussian with distribution smearing in the axial direction is recommended.[21] The physical representation of this can be seen in Figure 4

In eq. (8), an example of a 1D Gaussian distribution can be seen.

$$F_i^T(p_{1D}) = \frac{F_i^A}{\varepsilon_{1D}^2 \sqrt{\pi}} exp\left[-\left(\frac{p_{1D}}{\varepsilon_{1D}} \right)^2 \right] \tag{8}$$

In this 1D smearing, ε_{1D} is described by eq. (9). ε_i is recommended a value from 1 to 4.[21]

$$\varepsilon_{1D} = \varepsilon_i \Delta x \tag{9}$$

A 2D or 3D Gaussian distribution is usually used together with ALM. A 2D Gaussian distribution will not only smear the force in the axial direction but also in the azimuthal direction following a constant radius. So the force will not only be applied to the flow axially as in Figure 4 but also in azimuthal direction in the rotor plane as shown in Figure 5.

A 2D Gaussian distribution can be seen in eq. (10). The variable p_{2D} is the distance from the actuator point to the node on the line with the same radius.

$$F_i^T(p_{2D}) = \frac{F_i^A}{\varepsilon_{2D}^3 \pi} exp\left[-\left(\frac{p_{2D}}{\varepsilon_{2D}} \right)^2 \right] \tag{10}$$

FIGURE 4 Physical representation of a 1D Gaussian distribution in the streamwise direction used together with ADM
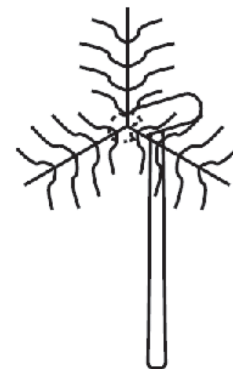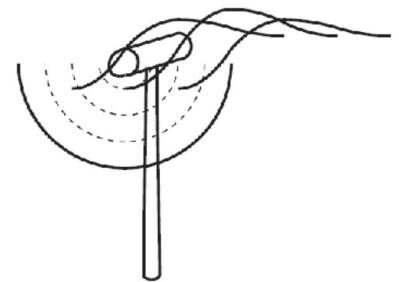
FIGURE 5 2D Gaussian distribution in addition to 1D Gaussian also apply forces in the rotor plane

The ε_{1D} in ADM is now not only a variable depending on the axial mesh resolution but the whole 3D mesh resolution and therefore renamed to ε_{2D}. Equation (11) shows the recommended formula for ε_{2D}.[21]

$$\varepsilon_{2D} = \varepsilon_i \sqrt{\left(R\Delta\theta^2\right)\Delta r^2 \Delta x^2} \tag{11}$$

A 3D Gaussian distribution can also be used. The force is then also applied along the radial direction of the actuator lines. This can physically be seen as spheres that increase in intensity the closer to the actuator point the cell is. The 3D Gaussian smears the force over the actual tip of the wind turbine blade. So when the tip flow behaviour has been investigated, a 2D Gaussian distribution has been preferred instead.[21] A 3D Gaussian distribution in shown in eq. (12).[17,23]

$$F_i^T(r) = \frac{F_i^A}{\varepsilon_{3D}^3 \pi^{3/2}} exp\left[-\left(\frac{r}{\varepsilon_{3D}}\right)^2\right] \tag{12}$$

The ε_{3D} has been recommended to be twice the cell axial length near the actuator line.[20] Independent of which Gaussian distribution that is chosen, the choice of ε and cell size has been shown to have an impact on the results and have to be chosen with care.[17,21,22,24,25]

1.7 | SOWFA by NREL

The Simulator fOr Wind Farm Applications (SOWFA) developed by the National Renewable Energy Laboratory (NREL) has been used throughout this work.[17,26] SOWFA is a CFD solver that links the FAST version 7 code which is an aero elastic solver developed by NREL to OpenFOAM that models the wind.[27] This is done by replacing the momentum part of the BEM theory in FAST by CFD. FAST evaluates the structural and system response including blade deflection of the wind turbine and sends the aerodynamic forces back to the CFD. SOWFA is based on two way coupling between OpenFOAM and FAST.

The transport equation for momentum used in SOWFA can be seen in eq. (13). The reference potential temperature θ_0 is set to 300 K. The two last terms are the actuator turbine model and the forest model contributions.

$$\frac{\partial \bar{u}_i}{\partial t} + \frac{\partial}{\partial x_j}\left(\bar{u}_j \bar{u}_i\right) = -2\varepsilon_{i3k}\Omega_3\bar{u}_k - \frac{\partial \tilde{p}}{\partial x_i} - \frac{1}{\rho_0}\frac{\partial}{\partial x_i}\bar{p}_0(x,y) - \frac{\partial}{\partial x_j}\left(\tau_{ij}^D\right) - g\left(\frac{\bar{\theta}-\theta_0}{\theta_0}\right)\delta_{i3} + \frac{1}{\rho_0}f_i^T + F_{f,i} \tag{13}$$

SOWFA includes the Coriolis force seen in equation 13. The rotational rate vector at the latitude ϕ of the location on the planetary surface in this case Ryningsnäs at $57.2761°$ is evaluated by eq. (14).

$$\Omega_j = \omega \begin{bmatrix} 0 \\ cos\phi \\ sin\phi \end{bmatrix} \tag{14}$$

The transport equation of the potential temperature is given in eq. (15). The last term is the heat source in the forest model.

$$\frac{\partial \bar{\theta}}{\partial t} + \frac{\partial}{\partial x_j}\left(\bar{u}_j\bar{\theta}\right) = -\frac{\partial}{\partial x_j}\left(q_j\right) + S_h \tag{15}$$

Neutral stratification is simulated in the present study. A capping inversion is used to control the height of the boundary layer. The centre of the capping inversion is located on a height of 450 m; it increases by 8 K over a height of 10 m. SOWFA can only use LES. The sub grid model is the Smagorinsky model.[28] The Smagorinsky constant is set to 0.13, and the filter width is set to the cube root of the cell volume.[17] This model has been shown to be over dissipative near the ground.[29] However, the implementation done by the developers of SOWFA has been shown to be less dissipative near the walls than the standard implementation in OpenFOAM.[17] The wall model was developed by Schumann.[30] The ALM model is used as an actuator turbine model with a 3D Gaussian distribution function using ε as twice the cell size.[20] This has been found to be the minimum value to avoid oscillations.[17]

The work flow with SOWFA is to first run an atmospheric boundary layer simulation without any wind turbines and using only cyclic boundary condition. This simulation is in this work used as a precursor simulation but could also be used stand alone. When the flow is considered to be fully developed, planes in the computational domain are saved. The flow is considered to be fully developed after more than 10 flow passes, this

is because no trace of the initializing was seen. These are later used as inlet boundary condition in the simulation that includes wind turbines. The main advantage with this procedure is that the flow is fully developed at the inlet in the wind turbine simulation. In the following simulations, the wind turbine are introduced, and OpenFOAM is coupled to FAST.[31] In this work, the data obtained from FAST are processed using the rain flow counting algorithm to obtain the fatigue loads.[32]

2 | RESULTS

To be able to validate and investigate the implementations in SOWFA, the test site of Ryningsnäs is used. The following LES simulations are made in the present study.

1. Homogeneous forest.
   a. No wind turbine (Atmospheric boundary layer simulation)
   b. Wind Turbine 2
   c. Wind Turbines 1 and 2
2. Current clearing
   a. No wind turbine (Atmospheric boundary layer simulation)
   b. Wind Turbine 2
   c. Wind Turbines 1 and 2
3. Extended clearing
   a. No wind turbine (Atmospheric boundary layer simulation)
   b. Wind Turbine 2
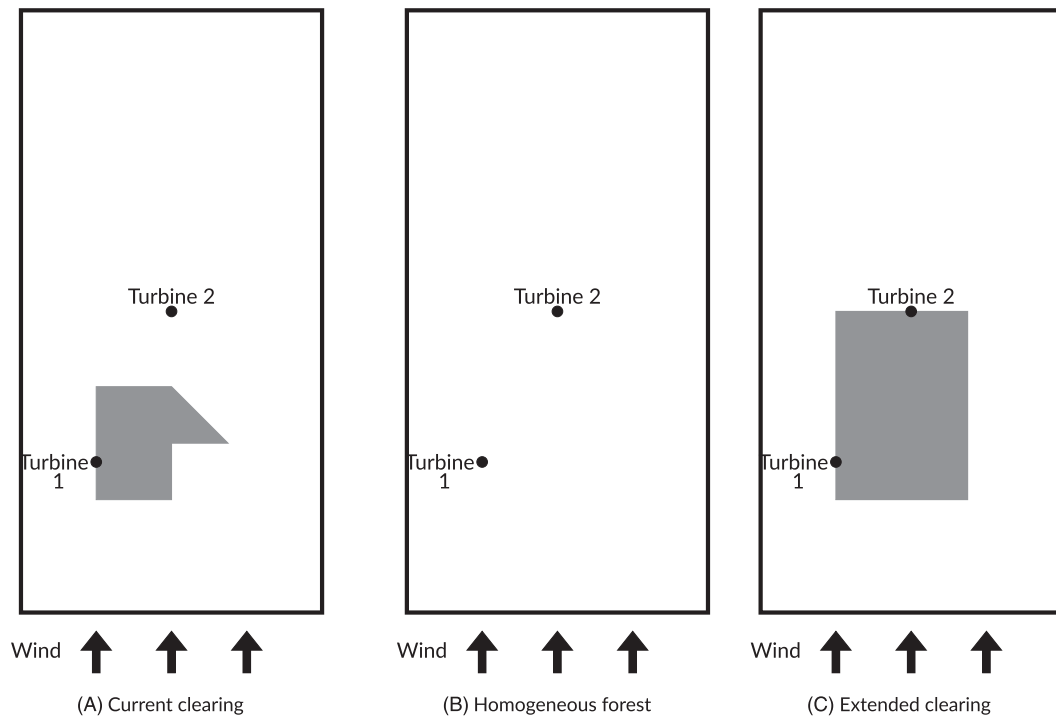   c. Wind Turbines 1 and 2

The atmospheric boundary layer simulations are validated against the data from an extensive measurement campaign performed at Ryningsnäs.[33,34]

2.1 | Ryningsnäs

The Ryningsnäs test site is simulated with the wind blowing from the south. The wind turbine after the clearing is located within 22 forest heights after the clearing which is the forest effecting distance.[8] The computational domain seen from above can be seen to the left in Figure 6. The forest is in white and the clearing in grey; the locations of the two wind turbines at the site are also shown. Wind Turbine 1 is located on the west side of the clearing 100 m into the clearing along the flow direction. Wind Turbine 2 is located 200 m along the east direction and 800 m along the flow direction into the clearing. The distance between the south side of the clearings and the inlet is 300 m. The measurements used in the comparison are from a metmast located in the northwest corner of the current clearing.[33,34] In all the simulations, the 5-MW wind turbines from NREL is used, because no data for the wind turbines at the location are available.[31] To be able to draw any general conclusions of the shape of the clearing and its effects on the wind turbines, one more clearing is investigated. This clearing has the maximum width of the current and extends until the second turbine. This clearing is called the extended clearing and can be seen to the right in Figure 6. Both the clearings are larger than five forest heights in the streamwise direction. This means that the flow always show edge effects.[10] To be able to distinguish the effects of the clearings, a setup with homogeneous forest is also investigated, and its domain can be seen in the middle of Figure 6. It should be noted that wind blowing from the south is along the y axis in SOWFA because of the Coriolis force and the simulations was setup like this in SOWFA. But to increase the readability of this paper, the flow direction will be referred to as the positive x axis. To avoid speed up of the flow, the width of the computational domain was chosen as 3.5 times the height.[35] This resulted in that the computational domains have a width (y direction) of 2800 m, a length (x) of 1600 m and a height (z) of 800 m.

The average forest height h is used in the simulations; at Ryningsnäs, it is 20 m.[12] The forest is modelled using the model by Shaw and Shumann; see eq. (1) and2. The forest at the Ryningsnäs site is made up of scots pine tree, and it is used to model the vertical area density.[19] The setup uses z_m of $0.6h$ and L_m of 0.37 to simulate scots pine tree.[18,19] The standard wall model in SOWFA was set to model grass plains below the forest using a value of 0.02 for the aerodynamic roughness height.[30,36] Wall functions are used on the ground where the friction velocity is obtained from

$$\tau_w = -\left(\frac{u_{par}\kappa}{\ln(z/z_0)}\right)^2 \tag{16}$$

FIGURE 6 (A–C) Current, homogeneous and extended computational domains. White is forest, and clearing in grey. The locations of the two wind turbines are shown with black bullets

where $u_{par} = (\bar{u}^2 + \bar{v}^2)^{1/2}$ is the instantaneous horizontal velocity magnitude in the wall-adjacent cells and $\kappa = 0.41$ is the von Karman constant.

2.2 | Atmospheric boundary layer without a clearing

The forest is in this section homogeneous. Periodic boundary conditions are used in the x and y directions. Symmetry boundary conditions are used at the top boundary, and wall functions are used on the ground (see equation 16). A driving pressure gradient is used in the streamwise direction (x) to ensure that the streamwise component of the velocity at hub height, 90 m, is 10 m/s. The time step is adjusted during the simulation to not exceed a Courant number of one. The simulation is run for 10 flow passes before starting to average, because no trace of the initialization was seen then. The results are then averaged during the following 50 flow passes. Fifty flow passes is used to have sufficient data to make the average value of the data converge. The flow fields in a y–z plane are stored every time step and are used as inlet boundary condition for the LES simulations with a clearing (see Section 2.3). It is well know that in LES simulations, this type of unsteady, turbulent inflow boundary condition from a precursor simulation is much better than a steady inlet boundary condition.[3] All the precursor simulations are using a width of 2800 m (y direction) and a height of 800 m (z direction) of the computational domains. The length is investigated to avoid turbulent streaks (regions with high or low streamwise velocity). The mesh resolution was 10 m along all directions in all the simulations, in order to resolve all the turbulent length scales that must be accurately predicted for the wind turbine simulations later on.[37] The time-averaged $\bar{u}$ velocity planes at hub height for the computational domain length of 1600, 3000, 5000 and 10 000 m can be seen in Figure 7. For the two shortest computational domains, streaks are clearly seen, with a large region in the middle, from inlet to outlet, with a high streamwise velocity. This means that the flow is affected by the short computational domain. The 3000-m setup is the shortest length recommended for SOWFA at neutral to lightly unstable stratification. In the present work (neutral stratification), a 3000-m long computational domain is too short, because thin regions of high velocity was found which extend from the inlet to the outlet. In the simulations with the two longest computational domains, no streaks are seen, so both are accepted to be used for creating inlet boundary condition. The 5000-m domain is chosen because of its lower computational cost.

2.3 | Atmospheric boundary layer with a clearing

Inlet conditions at the lower boundary (low x) in Figure 6 are set by using the stored data from the homogeneous simulations in Section 2.2. Neumann outlet boundary conditions are used at the upper boundary (high x) in Figure 6. Periodic boundary conditions are set at the side boundaries (low y and high y) and symmetric boundary conditions are prescribed at the top boundary (high z).

2.3.1 | Simulations without wind turbines

To investigate the flow field without any wind turbines, x–z planes in the middle of the clearing are chosen for the analysis. The grid, the time step and the number of time steps are the same as in Section 2.2. The time-averaged velocity $\bar{u}$ is shown in Figure 8, $\bar{v}$ velocity in Figure 9 and $\bar{w}$ velocity in Figure 11. The homogeneous forest is located in the middle of each figure, the current clearing is above and the extended clearing is below. In the homogeneous forest, the wind is, as expected, blowing along the forest with a constant boundary layer height. The $\bar{u}$ velocity is increasing close to the ground in the downstream part of the extended clearing seen in Figure 8. In the current clearing, the flow is not affected as much by the clearing as in the extended clearing. After the clearings, the flow on top of the forest is accelerating seen by that the white contour line moves closer to the ground. The flow then starts to build a new boundary layer above the forest.

The $\bar{v}$ velocity is mainly affected in the case of the current clearing; see Figure 9. The reason is that the current clearing is not symmetric along flow direction in the clearing, as in the case of the extended clearing. In the end of the current clearing, the flow is also moving more to the east (negative $\bar{v}$) than what is seen in the case of the extended clearing.

The wind flow at the location of the wind turbines are shown in Figure 10 by looking at the horizontal velocity ($U_l = \sqrt{\bar{u}^2 + \bar{v}^2}$) normalized by the friction velocity ($u_* = \langle \overline{u'v'}^2 + \overline{v'w'}^2 \rangle^{1/4}$; the friction velocity is evaluated at two forest heights at the location of the wind turbines in each clearing). The velocity at the first wind turbine in all cases and also for Wind Turbine 2 in the homogeneous forest is more or less the same in all the simulations. This is not that surprising since the flow has mainly travelled along homogeneous forest before reaching this wind turbine. The location of the wind turbine after the clearing in the extended clearing (Wind Turbine 2) has the highest velocity at the bottom of the rotor plane and
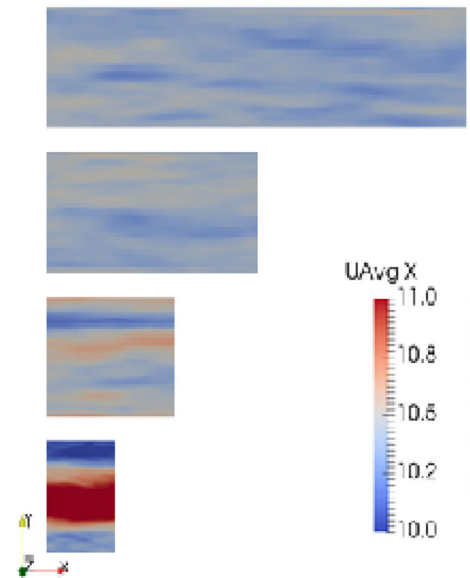

FIGURE 7 Planes of the time-averaged $\bar{u}$ velocity for the precursor simulations at hub height. The streamwise extent of the computation domain is, from bottom to top: 1500, 3000, 5000 and 10 000 m
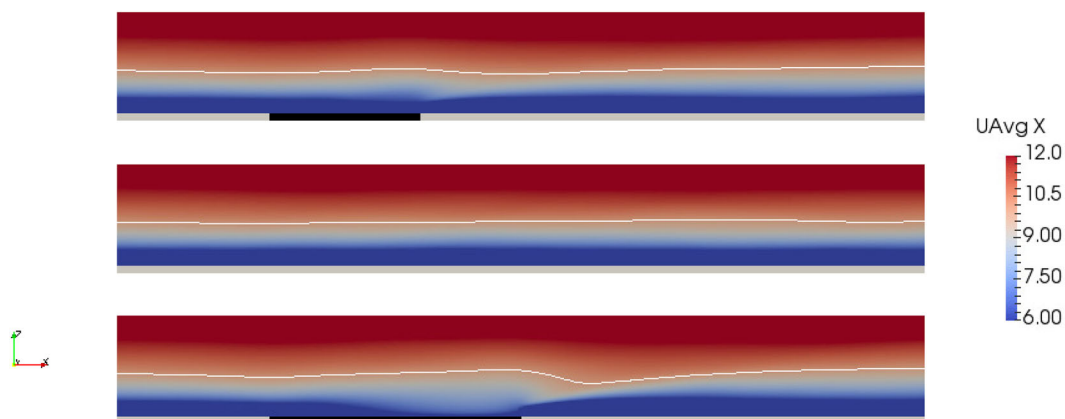
FIGURE 8 Time-averaged $\bar{u}$ in LES simulation with a clearing. $y = 400$ m. Contour line in white shows time-averaged $\bar{u} = 10$ m/s. From the top to bottom: current clearing, no clearing and extended clearing. Below each figure, the location of the clearing is marked in black
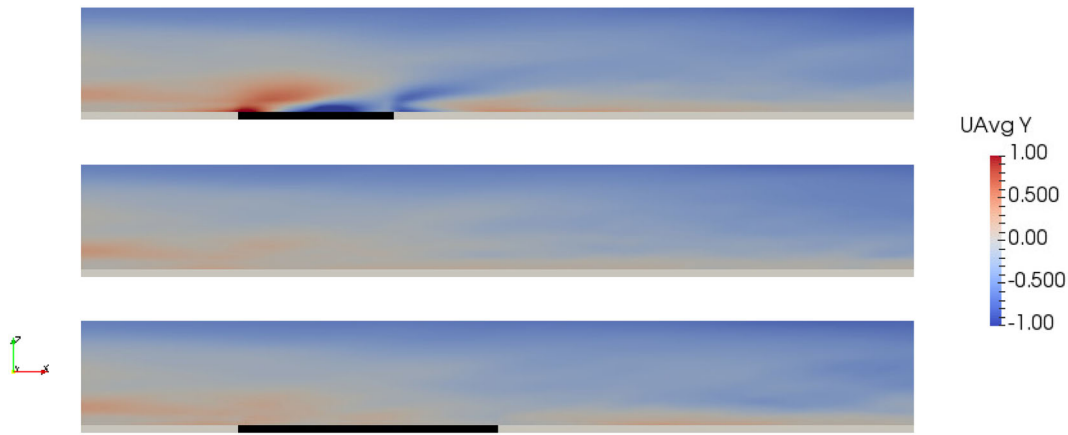
FIGURE 9 Time-averaged $\bar{v}$ velocity in the middle of the clearing. From the top to bottom: current clearing, no clearing and extended clearing. Below each plane, the location of the clearing is marked in black
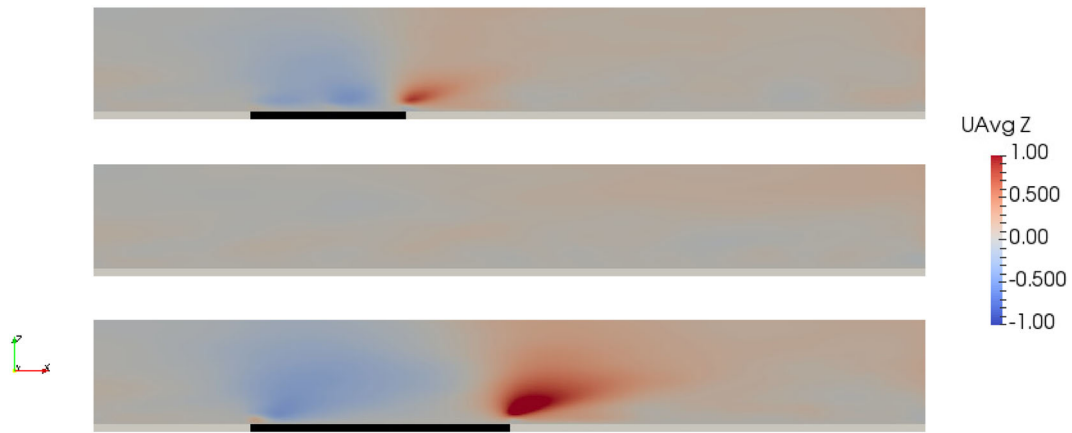

(A) Global view   (B) Zoom in rotor plane
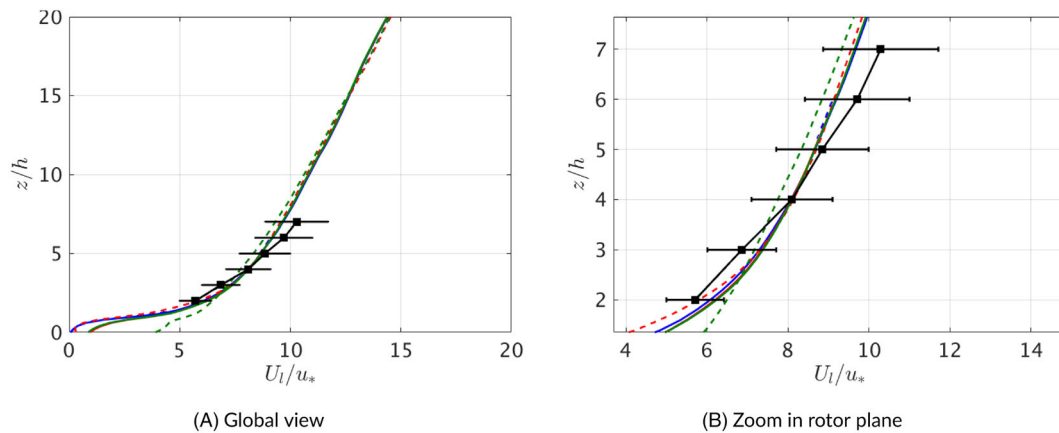
FIGURE 10 (A,B) $\langle U_l/u_* \rangle$ at the location of the wind turbines. ——: Wind Turbine 1 in homogeneous forest, – –: Wind Turbine 2 in homogeneous forest, ——: Wind Turbine 1 in current clearing, – –: Wind Turbine 2 in current clearing, ——: Wind Turbine 1 in extended clearing, – –: Wind Turbine 2 in extended clearing, ■: measurements[33,34]

the lowest velocity at the top of the rotor plane. Hence, this wind turbine location has the flattest velocity profile of them all, that is, the lowest wind shear. All the simulations are within the margin of the measurements; however, the measurements have a steeper gradient. This difference is assumed to be because the no blockage effect from the wind turbines are seen, because no wind turbines are located in the simulations at this phase.

When looking at the $\bar{w}$ velocity in Figure 11, the flow is moving downwards into the clearing after the forest edge and upwards after the clearings. This velocity is the strongest in the case of the extended clearing because the clearest disrupting of the forest boundary layer before the clearing is seen here. This is consistent with what is observed for the $\bar{u}$ velocity.

The vertical turbulent flux of streamwise momentum can be seen in Figure 12. In the rotor plane, all forest types for Wind Turbine 1 are very similar. Inside the forest, the extended clearing shows a bit higher vertical momentum flux than the other cases. This is probably due to the larger clearing surrounding this wind turbine in the extended clearing. For the location of Wind Turbine 2, the homogeneous forest has the highest vertical momentum flux, that is, the same as for Wind Turbine 1. The current clearing has the lowest vertical momentum flux. The vertical momentum flux for the extended clearing has a different shape and decreases a lot at four forest heights. This is because the flow has adapted to the clearing. Wind Turbine 2 in the current clearing is the one that should be closest to the measurements because it is located closest to the metmast and it is within acceptable margin.

The variance of the $\bar{u}$ velocity can be seen in Figure 13, for the $\bar{v}$ velocity in Figure 14 and for the $\bar{w}$ velocity in Figure 15. The streamwise variance, $\langle u'u'/u_*^2 \rangle$ is the largest. For Wind Turbine 1, the streamwise variance for the current and extended clearing are similar, but for the homogeneous forest, it is a bit higher in the rotor plane and slightly lower below the rotor plane for both the wind turbines. For Wind Turbine 2 in the current and extended clearings, the trends are the same as for $-\langle u'w'/u_*^2 \rangle$. The metmast is located in the northwest corner of the current clearing and Wind Turbine 2 is located north of the clearing explaining their difference in shape because the wind is adapting to the forest in between.

FIGURE 11 Time-averaged $\bar{w}$ velocity in the middle of the clearing. From the top current clearing, homogeneous forest and extended clearing. Below each plane, the location of the clearing is marked in black
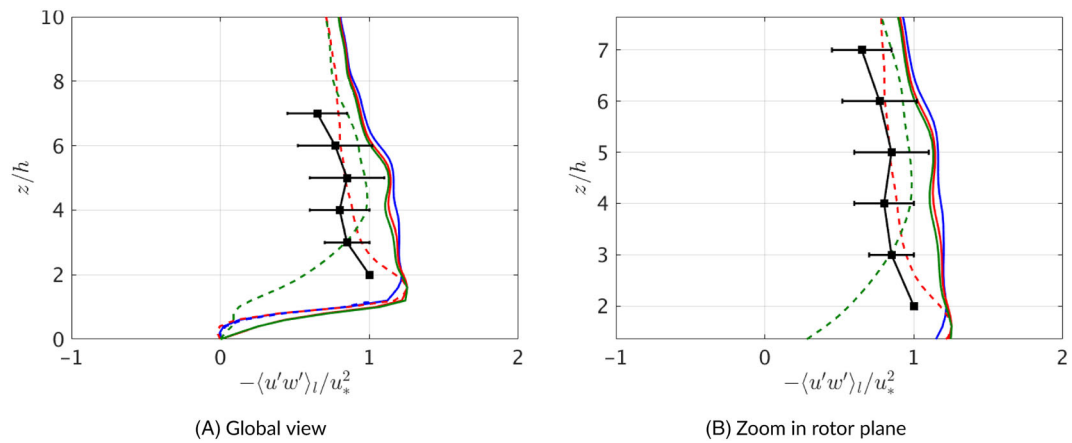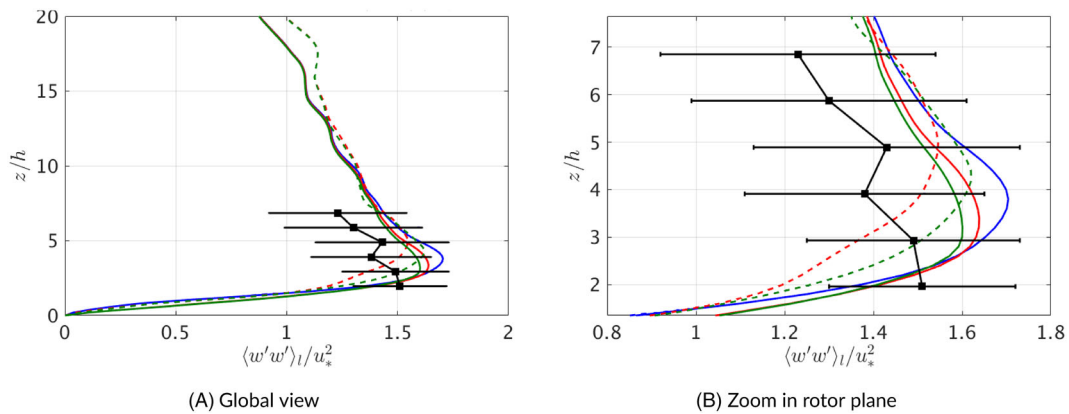

(A) Global view

(B) Zoom in rotor plane

FIGURE 12 (A,B) $-\langle u'w'/u_*^2\rangle$ at the location of the wind turbine. ——: Wind Turbine 1 in homogeneous forest, – –: Wind Turbine 2 in homogeneous forest, ——: Wind Turbine 1 in current clearing, – –: Wind Turbine 2 in current clearing, ——: Wind Turbine 1 in extended clearing, – –: Wind Turbine 2 in extended clearing, ▬■▬: measurements[33,34]

(A) Global view

(B) Zoom in rotor plane
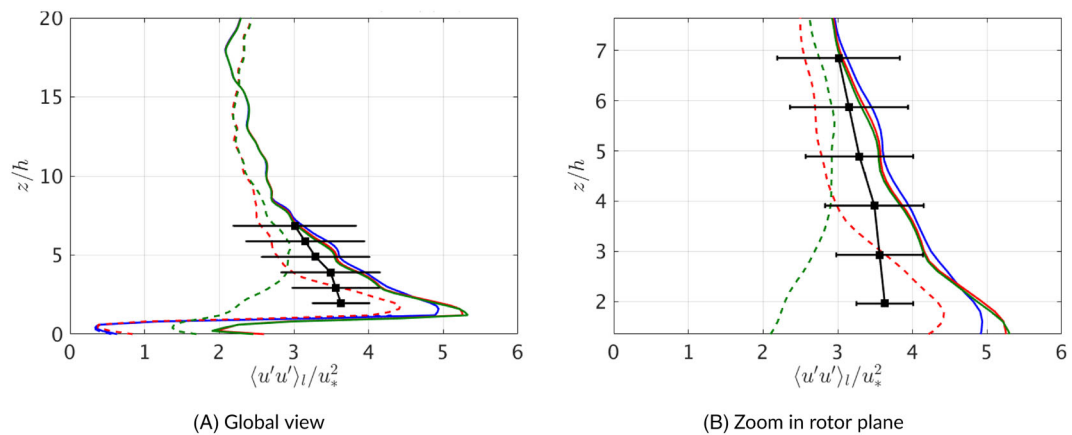
FIGURE 13 (A,B) $\langle u'u'/u_*^2\rangle$ at the location of the wind turbine. ——: Wind Turbine 1 in homogeneous forest, – –: Wind Turbine 2 in homogeneous forest, ——: Wind Turbine 1 in current clearing, – –: Wind turbine 2 in current clearing, ——: Wind Turbine 1 in extended clearing, – –: Wind Turbine 2 in extended clearing, ▬■▬: measurements[33,34]
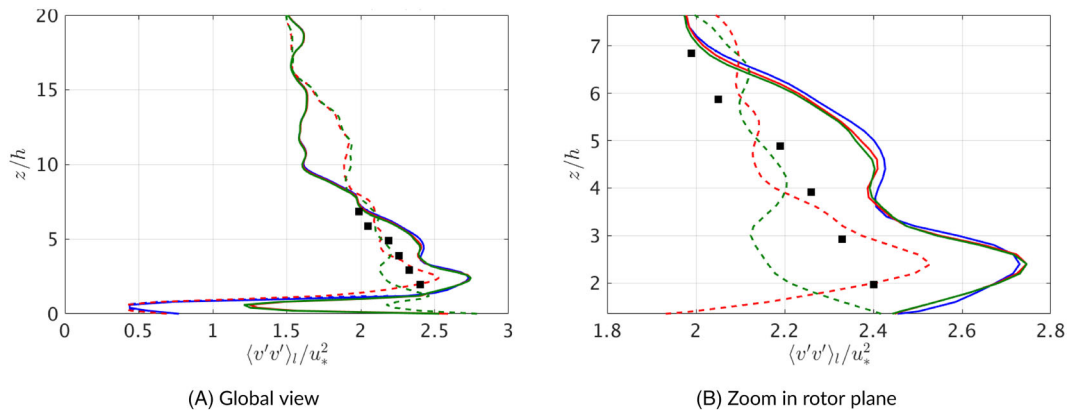
FIGURE 14 (A,B) $\langle v'v'/u_*^2 \rangle$ at the location of the wind turbine. ——: Wind Turbine 1 in homogeneous forest, – –: Wind Turbine 2 in homogeneous forest, ——: Wind Turbine 1 in current clearing, – –: Wind Turbine 2 in current clearing, ——: Wind Turbine 1 in extended clearing, – –: Wind Turbine 2 in extended clearing, —■—: measurements (no data for error bars available)[33,34]

FIGURE 15 (A,B) $\langle w'w'/u_*^2 \rangle$ at the location of the wind turbine. ——: Wind Turbine 1 in homogeneous forest, – –: Wind Turbine 2 in homogeneous forest, ——: Wind Turbine 1 in current clearing, – –: Wind Turbine 2 in current clearing, ——: Wind Turbine 1 in extended clearing, – –: Wind Turbine 2 in extended clearing, —■—: measurements[33,34]

For $\langle v'v'/u_*^2 \rangle$ (see Figure 14), at the location of Wind Turbine 1, the trends are the same as for $-\langle u'w'/u_*^2 \rangle$ but with lower magnitudes. All cases are very similar in the upper part of the rotor plane. But in the lower part and close to the ground, the results differ a lot. The variance in the homogeneous forest is again nearly identical for Wind Turbines 1 and 2. For Wind Turbine 2 in the current clearing, the variance has a bit lower magnitude but the same shape. But the shape at Wind Turbine 2 for the extended clearing is the lowest of them all in the lower region of the rotor location, but it is then not decreasing as much as the other cases in the forest region. The reason is probably because the wind here has adapted to the longer clearing, and thereby, the effect of the forest can no longer be seen.

Within the forest all the simulations predict a similar $\langle w'w'/u_*^2 \rangle$ profile, see Figure 15. For Wind Turbine 1, in the rotor plane, the variance for the homogeneous forest has the highest values followed by the current clearing and the extended clearing. The second wind turbine in the homogeneous again predicts the same values as for Wind Turbine 1. The lowest values of Wind Turbine 2 is for the current clearing, and the highest values are seen for the homogeneous forest, but the magnitude is lower than both $\langle u'u'/u_*^2 \rangle$ and $\langle v'v'/u_*^2 \rangle$.

The turning angle can be seen in Figure 16. It is defined as positive when the flow is moving east. Ryningsnäs is located on the northern hemisphere, and due to this, the Coriolis force will deflect the wind to the east which agrees to what is predicted by all the simulations. Wind Turbine 1 is located at the edge of the forest in the current and extended clearing. Along the rotor location, it can be seen that this will cause the wind to deflect more to the east, that is, more towards Wind Turbine 2 than in the homogeneous forest. For the location of Wind Turbine 2, the homogeneous forest predicts values close to Wind Turbine 1. The turning angle of the current clearing changes most, and the reason is probably because of the more complex shape of the current clearing.

2.3.2 | Simulations including wind turbines

Next, SOWFA is used that couple the LES simulations with FAST using the ALM to model the effect of the wind turbines on the flow field. FAST predicts the structural response of the rotor blades, tower and so forth. The deflection of the rotor blades are fed back to the LES simulations through moving ALM forces through a Gaussian distribution. The grid is the same as in Section 2.2.[37] However, the time step is much smaller to avoid that the rotor blades move through too many cells in one time step. The electrical generator power from FAST for the two wind turbines is seen in Table 1. The first row in Table 1($\langle U \rangle^3$) shows OpenFOAM simulations without any turbines, that is, atmospheric boundary layer simulations. This expression is obtained by applying the momentum theory. The $\langle U \rangle$ is the integrated U velocity over the swept area of the blades, that is, the rotor plane, and will be the only variable changing between the different setups simulated. The second row presents OpenFOAM coupled to FAST simulations with only Wind Turbine 2, and the last row is from OpenFOAM coupled to FAST simulations in which both wind turbines are included. In order to facilitate comparison between homogeneous forest, current clearing and extended clearing the numbers at each line are related to Wind Turbine 2 in the homogeneous forest.

For the first wind turbine, FAST estimates a higher power than the integrated U^3. No measurements are available for validation, but since the results from FAST coupled to the LES simulations include more physics, these results are assumed to be more correct than simply evaluating U^3 at the location of the wind turbine.

The increase in estimated power for the second wind turbine compared to the second wind turbine in the homogeneous forest is highest in the atmospheric simulations for both clearings (i.e., first row) followed by the FAST simulations with only the second wind turbine (second row) and the simulations with both the wind turbines (third row) give the smallest increase (for the extended clearing, it actually gives a decrease). The decrease in power of the second wind turbine with the extended clearing in the simulations with both wind turbines compared to only one wind turbine shows that the first wind turbine has a large effect on the second wind turbine when the wind is blowing from the south. When comparing the two clearings with the homogeneous case, Rows 1 and 3 show the same trend for the first wind turbine. This is also the case for the second wind turbine of the current clearing. But in the extended clearing, both FAST simulations of the second wind turbine show that the power is
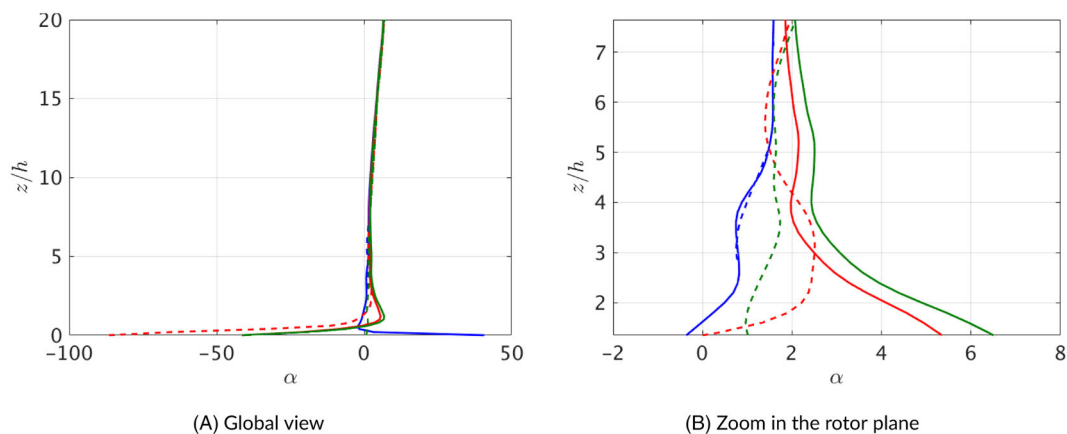
FIGURE 16 (A,B) Turning angle, α, at the location of the wind turbine. ——: Wind Turbine 1 in homogeneous forest, – –: Wind Turbine 2 in homogeneous forest, ——: Wind Turbine 1 in current clearing, – –: Wind Turbine 2 in current clearing, ——: Wind Turbine 1 in extended clearing, – –: Wind Turbine 2 in extended clearing, ▬■▬: measurements[33,34]

TABLE 1 Time-averaged electrical generator power evaluated using FAST

Electrical generator power	Homogeneous forest		Current clearing		Extended clearing	
	Turbine 1 (%)	Turbine 2 (%)	Turbine 1 (%)	Turbine 2 (%)	Turbine 1 (%)	Turbine 2 (%)
$\langle U \rangle^3$	+6.8	0.0[b]	+6.9	+4.3	+7.1	+1.0
FAST, only Turbine 2		0.0		+4.0		−2.5
FAST, both turbines	+8.4	0.0[a]	+8.3	+3.1	+8.3	−3.4

Note: For the atmospheric boundary layer simulations, $\langle U \rangle^3$ is integrated over the rotor plane.
[a]Wind Turbine 2 in the homogeneous forest when both wind turbines are in the simulation gives 3.3% higher power than when only wind turbine 2 is included in the simulation.
[b]Note that this 0 level cannot be compared to the 0 levels for the FAST results in the second and third rows.

lower than in the homogeneous forest whereas the atmospheric boundary layer simulation (first row) show the opposite. This shows the complexity of the problem and the importance of the FAST coupling.

The bending moment of the rotor has also been investigated using FAST. The time-averaged rotor bending around the *x* axis, that is, rotor torque, can be seen in Table 2. Because of the close relation between power and torque, the trends are the same as for the electrical generator power seen in Table 1. To evaluate the fatigue loads, the rain flow counting algorithm is used.[32] Figure 17 shows the rain flow of the rotor torque.

TABLE 2 Time-averaged rotor torque, that is, rotor bending moment around the *x* axis

	Homogeneous forest		Current clearing		Extended clearing	
Rotor torque	Turbine 1 (%)	Turbine 2 (%)	Turbine 1 (%)	Turbine 2 (%)	Turbine 1 (%)	Turbine 2 (%)
FAST, only Turbine 2		0.0		+2.5		−1.8
FAST, both turbines	+5.5	0.0[a]	+5.4	+2.0	+5.4	−2.3

[a]The torque for Wind Turbine 2 in the homogeneous forest when both wind turbines are included is 2.3% larger than when only Wind Turbine 2 is included.

(A) Both turbines (B) Only turbine 2
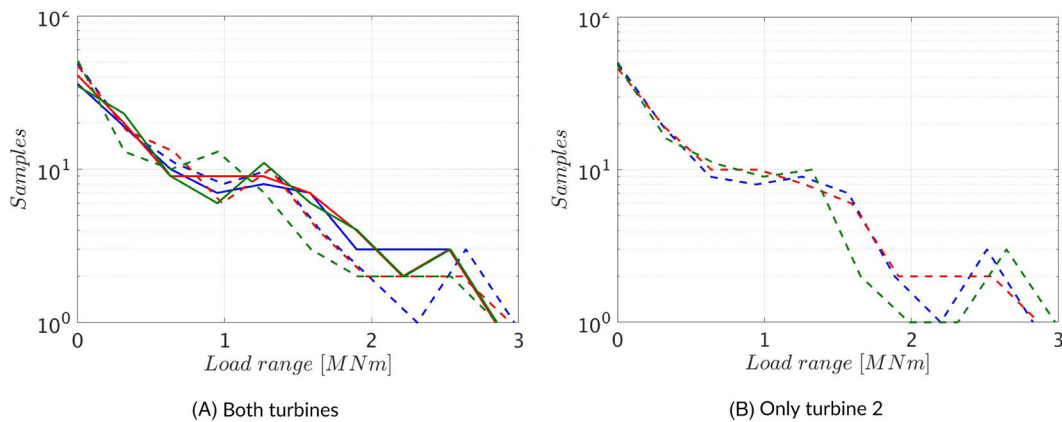
FIGURE 17 (A,B) Rain flow of rotor torque, that is, rotor bending moment around the *x* axis. ——: Wind Turbine 1 in homogeneous forest, – –: Wind Turbine 2 in homogeneous forest, ——: Wind Turbine 1 in current clearing, – –: Wind Turbine 2 in current clearing, ——: Wind Turbine 1 in extended clearing, – –: Wind Turbine 2 in extended clearing

(A) Both turbines (B) Only turbine 2
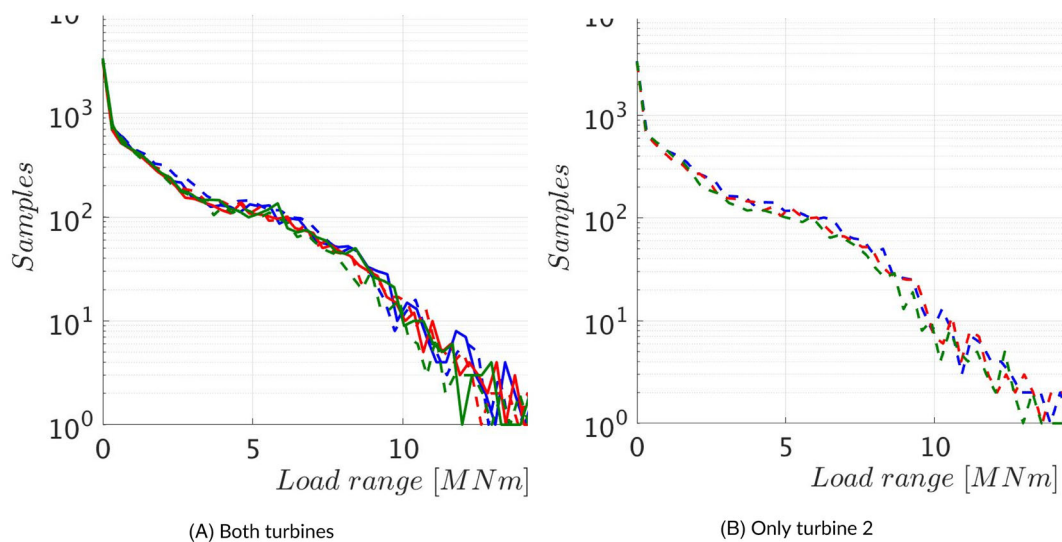
FIGURE 18 (A,B) Rain flow of rotor bending moment around the *y* axis. ——: Wind Turbine 1 in homogeneous forest, – –: Wind Turbine 2 in homogeneous forest, ——: Wind Turbine 1 in current clearing, – –: Wind Turbine 2 in current clearing, ——: Wind Turbine 1 in extended clearing, – –: Wind Turbine 2 in extended clearing

The fatigue loading is more or less the same for all three cases (homogeneous, current and extended clearing) irrespectively if the first wind turbine is included or not. But the load range of the rotor torque around the x axis is much lower than for the rotor bending around the y axis as can be seen in Figure 18 and around the z axis; see Matsfelt.[38] Hence, the rotor torque is not a limiting factor.

For the rotor bending moment around the y axis, the RMS values are evaluated and presented in Table 3. The reason for the difference in result for the first wind turbine in the homogeneous forest compared to the current and extended clearings is because the wind turbine is located on the edge of the forest in the clearing cases. This flattens the velocity profile in the region over the clearing and thus decreases the rotor bending moment around the y axis. Comparing the second wind turbine for the different cases shows that the current clearing has somewhat lower rotor bending moment around the y axis than the wind turbine in the homogeneous forest. Looking at the horizontal velocity in Figure 10, it can be seen that the current clearing has a somewhat flatter velocity profile except in the lowest part of the rotor location compared to the homogeneous forest. Wind Turbine 2 in the extended clearing has the lowest bending moment around the y axis of all cases. It can also be seen that the second wind turbine has the flattest velocity profile, that is, the lowest wind shear seen in Figure 10. Consider the fatigue loads in Figure 18 when only the second wind turbine is included. The general trend is that the homogeneous forest has the highest loading followed by the current

**TABLE 3** RMS of rotor bending moment around the y axis

Rotor bending moment around y axis	Homogeneous forest		Current clearing		Extended clearing	
	Turbine 1 (%)	Turbine 2 (%)	Turbine 1 (%)	Turbine 2 (%)	Turbine 1 (%)	Turbine 2 (%)
FAST, only Turbine 2		0.0		−0.4		−5.0
FAST, both turbines	+2.5	0.0^a	+1.0	−0.8	+1.0	−5.0

^{a}The bending moment for Wind Turbine 2 in the homogeneous forest when both wind turbines are included is 0.2% higher than when only Wind Turbine 2 is included.

TABLE 4 Time-averaged yaw bearing moment around the x axis

Yaw bearing moment around x axis	Homogeneous forest		Current clearing		Extended clearing	
	Turbine 1 (%)	Turbine 2 (%)	Turbine 1 (%)	Turbine 2 (%)	Turbine 1 (%)	Turbine 2 (%)
FAST, only Turbine 2		0.0		+2.4		−1.8
FAST, both turbines	+5.5	0.0^a	+5.3	+2.0	+5.3	−2.5

^{a}The yaw bearing moment for Wind Turbine 2 in the homogeneous forest when both wind turbines are included is 2.2% higher than when only Wind Turbine 2 is included.
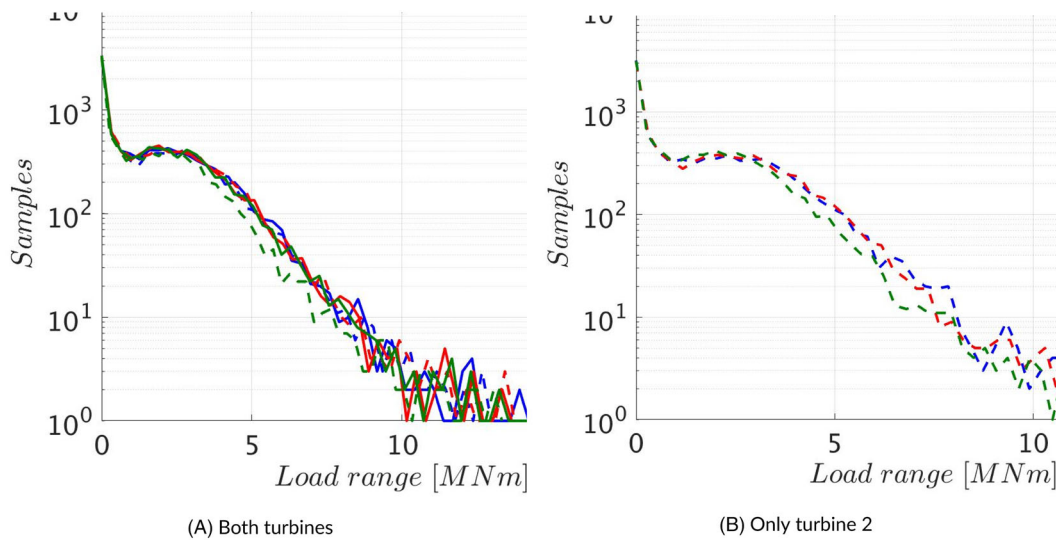

(A) Both turbines

(B) Only turbine 2
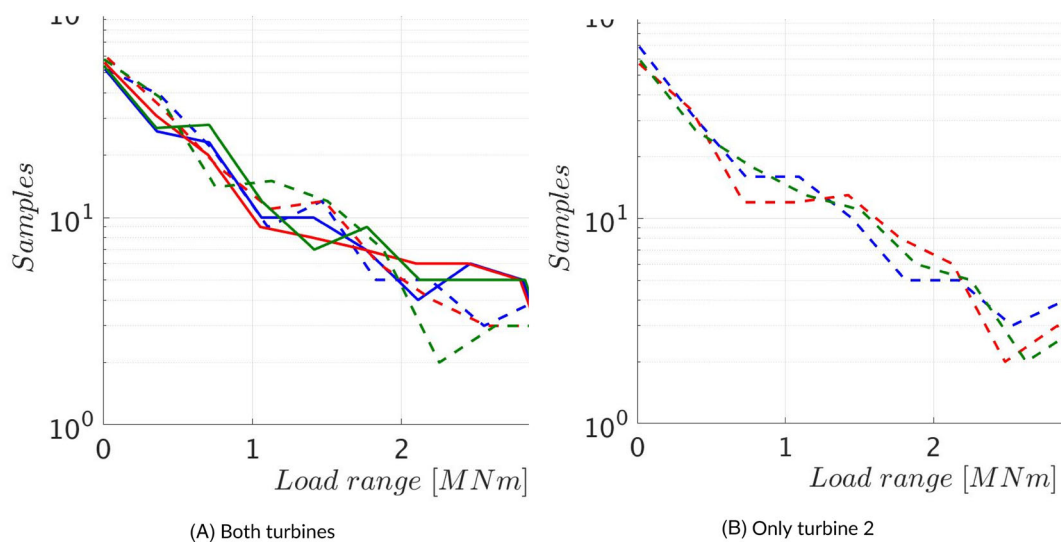
FIGURE 19 (A,B) Rain flow of yaw bearing moment around the x axis. ——: Wind turbine 1 in homogeneous forest, − −: Wind Turbine 2 in homogeneous forest, ——: Wind Turbine 1 in current clearing, − −: Wind Turbine 2 in current clearing, ——: Wind Turbine 1 in extended clearing, − −: Wind Turbine 2 in extended clearing

clearing, and the extended clearing has the lowest. When both wind turbines are included in the simulations, it gets more difficult to distinguish the results. But the second wind turbine in the extended clearing is generally the one with the lowest loading range. The trends for the RMS of the rotor bending and fatigue loads around the z axis are the same as those around the y axis.[38]

The yaw bearing is fixed in the simulations, and the bending moment is here investigated. The yaw bearing moment around the x axis is given in Table 4 and also here the trends are the same as for the electrical power and the rotor torque. The fatigue loads are seen in Figure 19 for the yaw bearing moment around the x axis. As seen for the rotor bending moment, the yaw bearing moment around the x axis is the lowest of the three and thereby not the limiting factor when comparing to moment around the y axis seen in Figure 20 and z axis seen in Figure 21.

For the yaw bearing bending around the y axis, the time-averaged values can be seen in Table 5. Here the two wind turbines in the homogeneous forest show rather similar values. The difference between Wind Turbines 1 and 2 increases as the clearing between them increases. When analysing Wind Turbine 2 with and without Wind Turbine 1 in the simulations with a clearing, the yaw bearing moment around the y axis always increases by approximately 2% for all cases when Wind Turbine 1 is included, that is, Wind Turbine 1 has a negative effect on Wind Turbine

(A) Both turbines   (B) Only turbine 2

FIGURE 20 (A,B) Rain flow of yaw bearing moment around the y axis. ——: Wind Turbine 1 in homogeneous forest, – –: Wind Turbine 2 in homogeneous forest, ——: Wind Turbine 1 in current clearing, – –: Wind Turbine 2 in current clearing, ——: Wind Turbine 1 in extended clearing, – –: Wind Turbine 2 in extended clearing

(A) Both turbines   (B) Only turbine 2
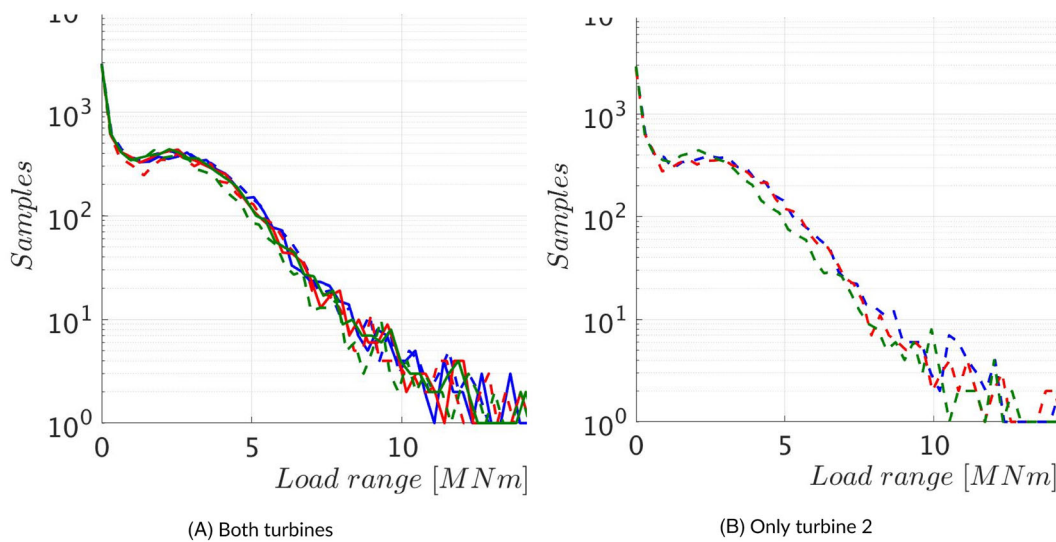
FIGURE 21 (A,B) Rain flow of yaw bearing moment around the z axis. ——: Wind Turbine 1 in homogeneous forest, – –: Wind Turbine 2 in homogeneous forest, ——: Wind Turbine 1 in current clearing, – –: Wind Turbine 2 in current clearing, ——: Wind Turbine 1 in extended clearing, – –: Wind Turbine 2 in extended clearing

TABLE 5 Time-averaged yaw bearing moment around y axis

Yaw bearing moment around y axis	Homogeneous forest		Current clearing		Extended clearing	
	Turbine 1 (%)	Turbine 2 (%)	Turbine 1 (%)	Turbine 2 (%)	Turbine 1 (%)	Turbine 2 (%)
FAST, only Turbine 2		0.0		−5.2		−20.2
FAST, both turbines	−0.4	0.0[a]	−5.0	−3.6	−5.9	−18.8

[a]The yaw bearing moment for wind turbine 2 in the homogeneous forest when both wind turbines are included is 1.3% higher than when only Wind Turbine 2 is included.

TABLE 6 Time-averaged yaw bearing moment around z axis

Yaw bearing moment around z axis	Homogeneous forest		Current clearing		Extended clearing	
	Turbine 1 (%)	Turbine 2 (%)	Turbine 1 (%)	Turbine 2 (%)	Turbine 1 (%)	Turbine 2 (%)
FAST, only Turbine 2		0.0		−14.1		−1.0
FAST, both turbines	−6.2	0.0[a]	−5.9	−23.7	−4.6	−7.1

[a]The yaw bearing moment for Wind Turbine 2 in the homogeneous forest when both wind turbines are included is 9.8% lower than when only Wind Turbine 2 is included.

2. The fatigue loads around the y axis seen in Figure 20 follow the same trends as seen before, with Wind Turbine 2 in the extended forest having the lowest fatigue load.

The time-averaged moment around the z axis for the yaw bearing can be seen in Table 6. Here Wind Turbine 2 in the current clearing has the lowest value. When looking at Figure 9, this is the wind turbine which experiences the largest variations in the $\bar{v}$ velocity. This shows that the shape of the clearing can have a positive influence on the wind turbines located close to a clearing. For the fatigue loads of the yaw bearing around the z axis seen in Figure 21, however, it is found that Wind Turbine 2 in the extended clearing is displaying the smallest load. This is somewhat surprising because of the large decrease in time-averaged value of Wind Turbine 2 in the current clearing seen in Table 6. This shows the importance of including not only the time-averaged values but also the fatigue loads in the analysis.

The in-plane and out-of-plane bending moment at the blade root, the tower base moment around the y axis can be found in Matsfelt.[38]

3 | CONCLUSIONS

The recommended computational domain length for SOWFA at neutral to lightly unstable stratification is in the literature 3000 m. For the precursor, this was found to be too short because streaks extending in the streamwise direction through the entire domain were found. A 5000-m long computational domain was needed to avoid the streaks.

From the atmospheric boundary layer simulations with a clearing and without wind turbines, it was seen that the streamwise $\bar{u}$ velocity is increasing in the downstream part of the extended clearing close to the ground. In the current clearing, the flow is not affected as much by the clearing. This shows the importance of choosing the correct length of the clearing with respect to which flow phenomena that are preferred. This was also consistent with observations for the vertical $\bar{w}$ velocity. A clearing can also be used to steer the wind in a preferred direction. This was seen from the $\bar{v}$ velocity that steers the flow to the east in the current clearing. When studying the location of the second wind turbine, the extended clearing had the lowest wind shear.

Wind Turbine 1 is located at the edge of the forest edge in the current and extended clearing. From the turning angle, the flow was seen to deflect more to the east, that is, into the clearing, and in this case also towards Wind Turbine 2.

When estimating the electrical power for the second wind turbine, integrated $\langle U^3 \rangle$ and FAST gave opposite trends. This shows the complexity of the problem and the importance of the FAST coupling. From the simulations including wind turbines, the electrical generator power of Wind Turbine 2 was found to be largest for the current clearing. But the fatigue loads were both higher and lower than the homogeneous forest depending on which part of the wind turbine that was investigated. The extended clearing nearly always had the lowest fatigue loads but unfortunately also the lowest electrical generator power. Further optimization of the clearings and the wind turbine locations in relation to them is needed to find the sweet spot where the fatigue loads are lower and the electrical generator power is higher.

ORCID

Johanna Matsfelt https://orcid.org/0000-0002-9441-1526
Lars Davidson https://orcid.org/0000-0003-2903-4004

REFERENCES

1. Nebenführ B, Davidson L. Influence of a forest canopy on the neutral atmospheric boundary layer—a LES study; 2014.
2. Zendehbad M, Chokani N, Abhari R. Impact of forested fetch on energy yield and maintenance of wind turbines. *Renew Energy*. 2016;96:548-558.
3. Mueller E, Mell W, Simeoni A. Large eddy simulation of forest canopy flow for wildland fire modeling. *Can J For Res*. 2014;44(12):1534-1544.
4. Dellwik E, Bingöl F, Mann J. Flow distortion at a dense forest edge. *Q J R Meteorol Soc*. 2014;140:676-686.
5. Dupont S, Brunet Y. Coherent structures in canopy edge flow: a large-eddy simulation study. *J Fluid Mech*. 2009;630(7):93-128.
6. Sogachev A, Leclrec M, Zhang G, Rannik U, Vesala T. CO_2 fluxes near a forest edge: a numerical study. *Ecol Appl*. 2008;18:1454-1469.
7. Kanani-Subring F, Raasch S. Spatial variability of scalar concentrations and fluxes downstream of a clearing-to-forest transition: a large-eddy simulation study. *Bound-Layer Meteorol*. 2014;155:1-27.
8. Dupont S, Bonnefond J-M, Irvine MR, Lamaud E, Brunet Y. Long-distance edge effects in a pine forest with a deep and sparse trunk space: in situ and numerical experiments. *Agric For Meteorol*. 2011;151(3):328-344.
9. Klaassen W, van Breugel P, Moors E, Nieveen J. Increased heat fluxes near a forest edge. *Theor Appl Climatol*. 2002;72(3-4):231-243.
10. Dupont S, Brunet Y. Edge flow and canopy structure: a large-eddy simulation study. *Bound-Layer Meteorology*. 2008;126(1):51-71.
11. Glazunov A, Stepanenko V. Large-eddy simulation of stratified turbulent flows over heterogeneous landscapes. *Atmos Ocean Physics*. 2015;51(4):403-415.
12. Nebenführ B, Davidson L. Large-eddy simulation study of thermally stratified canopy flow. *Bound-Layer Meteorol*. 2015;156(2):253-276.
13. Baldocchi DD, Meyers TD. Turbulence structure in a deciduous forest. *Bound-Layer Meteorol*. 1988;43:345-364.
14. Dupont S, Brunet Y. Simulation of turbulent flow in an urban forested park damaged by a windstorm. *Bound-Layer Meteorol*. 2006;120(1):133-161.
15. Mohr M, Arnqvist J, Abedi H, Alfredsson H, Baltscheffsky M, Bergström H, Carlen I, Davidson L, Segalini A, Soderberg S. Wind power in forests II. Uppsala University; 2018.
16. Ivanell S, Arnqvist J, Avila M, Cavar D, Chavez-Arroyo RA, Olivares-Espinosa H, Peralta C, Adib J, Witha B. Microscale model comparison (benchmark) at the moderate complex forested site Ryningsnäs. *J Wind Energy Sci*. 2018;3:929-949.
17. Churchfield M, Lee S, Moriarty P. Overview of the simulator of offshore wind farm application, webinar. Webinar. NREL; 2012.
18. Shaw R, Shumann U. Large-eddy simulation of turbulent flow above and within a forest. *Bound-Layer Meteorology*. 1992;61(1):47-64.
19. Lalic B, Mihailovic D. An empirical relation describing leaf area density inside the forest for environmental modeling. *Journal of Applied Meteorology*. 2004;43(4):641-645.
20. Troldborg N. Actuator line modeling of wind turbine wakes. *PhD Thesis*, Technical University of Denmark; 2008.
21. Mikkelsen R. Actuator disc methods applied to wind turbines. Technical University of Denmark; 2003.
22. Martinez L, Leonardi S, Churchfield M, Moriarty P. A comparison of actuator disk and actuator line wind turbine models and best practices for their use; 2012.
23. Sørensen JN, Shen WZ. Numerical modeling of wind turbine wakes. *J Fluid Eng*. 2002;124:393-399.
24. Sørensen JN, Shen WZ, Munduate X. Analysis of wake states by a full-field actuator disc model. *Wind Energy*. 1998;1:73-88.
25. Matsfelt J. Actuator turbine models and trailing edge flow: implementation in an in-house code. *Master Thesis*, Chalmers University of Technology; 2015.
26. Fleming P, Gebraad P, Lee S, van Wingerden J-W, Johnson K, Churchfield M, Michalakes J, Spalart P, Moriarty P. Evaluating techniques for redirecting turbine wakes using SOWFA. *Renew Energy*. 2014;70:211-218.
27. OpenFOAM. User guide. https://cfd.direct/openfoam/user-guide/
28. Smagorinsky J. General circulation experiments with the primitive equations. *Mon Weather Rev*. 1963;91:99-164.
29. Porte-Agel F, Meneveau C, Parlange M. A scale-dependent dynamic model for large-eddy simulation: application to a neutral atmospheric boundary layer. *J Fluid Mech*. 2000;415:261-284.
30. Schumann U. Subgrid-scale model for finite-difference simulations of turbulent flow in plane channels and annuli. *J Comput Phys*. 1975;18:76-404.
31. Jonkman J, Butterfield S, Musial W, Scott G. Definition of a 5-MW reference wind turbine for offshore system development. NREL; 2009.

32. ASTM. Standard practices for cycle counting in fatigue analysis. American Society for Testing and Materials; 1985.

33. Bergström H, Alfredsson H, Arnqvist J, Carlen I, Dellwik E, Fransson J, Ganander H, Mohr M, Segalini A, Söderberg S. Wind power in forests: wind and effects on loads. Elforsk report; 2013.

34. Arnqvist J, Segalini A, Dellwik E, Bergström H. Wind statistics from a forested landscape. *Bound-Layer Meteorol*. 2015;156:53-71.

35. Bechmann A. Large-eddy simulation of atmospheric flow over complex terrain. *PhD Thesis*. Roskilde, Denmark; 2006.

36. Stull R. An introduction to boundary layer meteorology; 1988.

37. Martinez-Tossas L, Churchfield M, Leonardi S. Large eddy simulations of the flow past wind turbines: actuator line and disk modeling. *Wind Energy*. 2015;18:1047-1060.

38. Matsfelt J. Large eddy simulation of clearings in forest and their effect on wind turbines. Göteborg, Sweden; 2018.